Remarkable bismuth-gold alloy decorated on MWCNT for glucose electrooxidation: the effect of bismuth promotion and optimization via response surface methodology

Ömer Faruk ER[1] , **Berdan ULAŞ**[2],* , **Hilal DEMİR KIVRAK**[3]

[1]Department of Chemical Engineering, Faculty of Engineering, Van Yüzüncü Yıl University, Van, Turkey
[2]Department of Mining Engineering, Faculty of Engineering, Van Yüzüncü Yıl University, Van, Turkey
[3]Department of Chemical Engineering, Faculty of Engineering and Architectural Sciences, Eskişehir Osmangazi University, Eskişehir, Turkey

Abstract: In this study, the carbon nanotube supported gold, bismuth, and gold-bismuth (Au/MWCNT, Bi/MWCNT, and Au-Bi/MWCNT) nanocatalysts were prepared with $NaBH_4$ reduction method at varying molar atomic ratio for glucose electrooxidation (GAEO). The synthesized nanocatalysts at different Au: Bi atomic ratios are characterized via *x-ray diffraction* (XRD), transmission electron microscopy (TEM), and N_2 adsorption-desorption. For the performance of AuBi/MWCNT for GAEO, electrochemical measurements are performed by using different electrochemical techniques namely cyclic voltammetry (CV), linear sweep voltammetry (LSV), chronoamperometry (CA), and electrochemical impedance spectroscopy (EIS). Monometallic Au/MWCNT exhibits higher activity than Bi/MWCNT with 256.57 mA/mg (0.936 mA/cm²) current density. According to CV results, $Au_{80}Bi_{20}$/MWCNT nanocatalyst has the highest GAEO activity with the mass activity of 320.15 mA/mg (1.133 mA/cm²). For $Au_{80}Bi_{20}$/MWCNT, central composite design (CCD) is utilized for optimum conditions of the electrode preparation. $Au_{80}Bi_{20}$/MWCNT nanocatalysts are promising anode nanocatalysts for direct glucose fuel cells (DGFCs).

Key words: Gold, bismuth, carbon nanotube, glucose, electrooxidation, response surface methodology (RSM)

1. Introduction

Energy is a vital and permanent need for human life and welfare [1–7]. Fuels such as formic acid [8–10], glucose (GA) [11], ethanol [12, 13], ethylene glycol [14], hydrazine [15], and methanol [16, 17] are principal sources. From these sources, GA is given great significance due to its advantages such as abundance in nature, cheapness, non-toxicity, and easy to transport [18–20]. As a result of complete oxidation of GA, 24 e⁻ are released [21]. However, the complete electrooxidation of GA has not been achieved yet. Complete oxidation of GA consists of a complex reaction sequence [22]. Glucose electrooxidation (GAEO) to gluconic acid reactions are given as follows [23, 24]:

Anode: $C_6H_{12}O_6 + 2OH^-$ $C_6H_{12}O_7$ $+H_2O$ $+2e^-$ (1)

Cathode: $0.5O_2$ $+H_2O$ $+2e^-$ $2OH^-$ (2)

Overall: $C_6H_{12}O_6 + 0.5O_2$ $C_6H_{12}O_7$ (3)

The development of anode catalysts with high GAEO activity is crucial for the commercialization of the direct glucose fuel cell. Hence, the anode catalyst performance of $Fe_{15}Pt_{85}$ [25], Ni-Fe [26], Ni-Co [27], Au [28], Pt [29], G-ITO [30], AgNi [31], Pd [32], $FeCo_2O_4$ [33], and Pd-Au [34] nanocatalysts have been investigated for direct GA fuel cells (DGFC). For instance, Chai et al. reported that Pd_3Cu-B/C nanocatalyst synthesized by a simple aqueous phase approach method had high GAEO activity and stability for GAEO reaction in fuel cell [35]. Likewise, Yan et al. stated that $Pd_{70}Au_{30}$ nanocatalyst prepared via modified pulse microwave-assisted polyol method had high current density [36]. Another study performed by Chai et al. on the synthesis of Pd-SnCoO$_x$/C nanocatalysts and investigation of their GAEO activities revealed that Pd-SnCoO$_x$/C had enhanced activity and outstanding stability with a great active surface area compared to Pd/C nanocatalyst [37]. Related literature was given in Table 1.

Herein, we aim to investigate the effect of Bi addition to Au in terms of GAEO activity. Thus, Au/MWCNT, Bi/MWCNT, and Au-Bi/MWCNT nanocatalysts were prepared via $NaBH_4$ reduction method, and these nanocatalysts were characterized by XRD, BET, and TEM. To investigate the effect of Bi promotion, GAEO activities of these nanocatalysts

* Correspondence: berdanulas@yyu.edu.tr

Table 1. Maximum current densities for GAEO values reported in literature.

Nanocatalyst	Maximum peak mA/cm²	Reference
Pd_3Rh/C	1.7	(38)
AuAg/C	3.75	(39)
Pd_3Sn_2/C	3.64	(40)
PtRu/C	2.74	(41)
PtBi/C	2.25	(42)
$Cu@Cu_2O\text{-}Pd$	1.15	(43)

are measured via cyclic voltammetry (CV), linear sweep voltammetry (LSV), chronoamperometry (CA), and electrochemical impedance spectroscopy (EIS). For $Au_{80}Bi_{20}$/MWCNT nanocatalyst, central composite design (CCD) was utilized for determining the optimum conditions of electrode preparation. The volume of nanocatalyst slurry (V_c, A), ultrasonication time of the nanocatalyst slurry (t_u, B), and the drying time of the electrode (t_d, C) were determined as independent variables.

2. Materials and method

All chemicals used were purchased from Sigma-Aldrich. Au/MWCNT nanocatalysts and Bi/MWCNT nanocatalysts were synthesized by $NaBH_4$ reduction method with $AuCl_3$ and $Bi(NO_3)_3.5H_2O$ metal as a precursor, respectively. Metal precursors were dissolved in deionized water and mixed with 0.1 g MWCNT by adding $NaBH_4$ at ratio of $NaBH_4$:Au (15:1). These mixtures were filtered and washed. Likewise, Au-Bi/MWCNT nanocatalysts were prepared by $NaBH_4$ reduction method at different Au:Bi ratios as 95:5, 90:10, 80:20, 70:30, 60:40, and 50:50.

Au/MWCNT, Bi/MWCNT, and $Au_{80}Bi_{20}$/MWCNT nanocatalysts were characterized via N_2 adsorption and desorption (Micromeritics 3Flex equipment Tristar II 3020), XRD (PANalytical Empyrean device-ray diffractometer with Cu Kα radiation (λ = 1.54056 Å)), and C-TEM (Hitachi HighTech HT7700 high re-transmission electron microscope operating at 120 kV).

All electrochemical properties of Au/MWCNT, Bi/MWCNT, and Au-Bi/MWCNT nanocatalysts were determined by CV, LSV, CA, and EIS in 0.5 M GA. A nanocatalyst ink was obtained by dispersing 3 mg nanocatalyst in 1 mL of Nafion. Then, 5 mL of nanocatalyst ink was transferred to glassy carbon electrode and dried. CV measurements were performed at –0.6 V to 0.8 V potentials at 50 mv s⁻¹ scan rate. Stability measurements were conducted by CA during 1000 s.

CCD was utilized for optimum conditions of the electrode preparation. The volume of nanocatalyst slurry (V_c, A), ultrasonication time of the nanocatalyst slurry (t_u, B), and the drying time of the electrode (t_d, C) are determined as independent variables. The maximum current density values obtained for GAEO were identified as the response. The error for the value of response was determined by 6 experiments at the middle levels of the parameters, and 20 sets of experiments were performed in total. Table 2 depicts the experimental points determined by Design Expert 7.0 and their corresponding response values, where, – 1, 0, and + 1 represent the lowest, central, and highest levels of the parameters. Interactions between independent parameters were statistically evaluated with analysis of variance (ANOVA), and the suitability of the proposed model was tested with the coefficient of determination (R^2).

3. Results and discussion

3.1. Characterization results

Characterizations of Au/MWCNT, Bi/MWCNT, and $Au_{80}Bi_{20}$/MWCNT nanocatalysts were performed with XRD, BET, and TEM. XRD patterns of MWCNT supported Au, Bi, and $Au_{80}Bi_{20}$ nanocatalysts were given in Figure 1. The diffraction peaks of Au and Bi were clearly seen in Figure 1. The diffraction peaks of C (0 0 2) and C (1 0 0) planes were observed at around 25.5° and 42.8° for all nanocatalysts, respectively. The presence of the C (0 0 2) indicates that the carbon in the structure is hexagonal carbon [44]. The (1 1 1), (2 0 0), (2 2 0), (3 1 1), and (2 2 2) facets of Au were obtained at 38.3°, 44.4°, 64.5°, 77.3°, and 81.9° 2θ values for Au/MWCNT. These peaks are specific crystallographic planes of the face-centered cubic (fcc) Au [45, 46] (Figure 1). The average diameter of the nanocatalysts can be achieved by using Scherrer's Equation [47,48]. The crystal size of Au/MWCNT was found as 19.08 nm. For Bi/MWCNT, the (0 0 2), (1 1 0), (1 0 2), (0 2 0), (0 1 4), and (1 2 2) facets of Bi were observed at 24°, 30.2°, 32.9°, 46.9°, 51.8° and 56.9° 2θ values, respectively (Figure 1). As clearly seen from Figure 1, all diffraction peaks of Au and Bi were observed for $Au_{80}Bi_{20}$/MWCNT nanocatalyst. These results depict that the face-centered cubic (fcc) of Au maintains its structure and increases the GAEO activity of the nanocatalyst by increasing the number of

Table 2. Experimental design of CCD and obtained responses.

	A	B	C	Response
Run	V_c	t_u	t_d	Specific activity
	µL	min	min	mA/cm^2
1	7.75 (0)	30.50 (0)	30.00 (+1)	0.89
2	0.50 (−1)	30.50 (0)	15.50 (0)	1.41
3	7.75 (0)	60.00 (+1)	15.50 (0)	0.94
4	15.0 (+1)	60.00 (+1)	30.00 (+1)	0.73
5	7.75 (0)	30.50 (0)	15.50 (0)	0.96
6	15.0 (+1)	1.00 (−1)	1.00 (−1)	0.66
7	7.75 (0)	30.50 (0)	15.50 (0)	1.02
8	15.0 (+1)	1.00 (−1)	30.00 (+1)	0.79
9	15.0 (+1)	60.00 (+1)	1.00 (−1)	0.83
10	15.0 (+1)	30.50 (0)	15.50 (0)	1
11	0.50 (−1)	1.00 (−1)	30.00 (+1)	0.6
12	7.75 (0)	30.50 (0)	1.00 (−1)	0.83
13	7.75 (0)	30.50 (0)	15.50 (0)	0.97
14	7.75 (0)	1.00 (−1)	15.50 (0)	0.55
15	0.50 (−1)	1.00 (−1)	1.00 (−1)	0.86
16	7.75 (0)	30.50 (0)	15.50 (0)	1.03
17	7.75 (0)	30.50 (0)	15.50 (0)	0.95
18	0.50 (−1)	60.00 (+1)	1.00 (−1)	1.21
19	0.50 (−1)	60.00 (+1)	30.00 (+1)	1.14
20	7.75 (0)	30.50 (0)	15.50 (0)	1.17

active sites of Bi. The crystal size of Au$_{80}$Bi$_{20}$/MWCNT nanocatalyst was found as 21.96 nm. Moreover, the average inter-planar distances of Au/CNT, Bi/CNT, and Au$_{80}$Bi$_{20}$/MWCNT nanocatalysts were calculated using Bragg's Law [49,50]. The 2θ values of Au (111) and Bi (110) peaks, which are the most intense peaks in the XRD patterns, were used. The average interplanar distance for Au/CNT, Bi/CNT, and Au$_{80}$Bi$_{20}$/MWCNT nanocatalysts was calculated as 2.35, 2.95, and 2.35 nm, respectively.

N$_2$ adsorption-desorption were used to determine pore size, BET surface area, and pore volume of Au/MWCNT, Bi/MWCNT, and Au$_{80}$Bi$_{20}$/MWCNT. BET surface area, pore size, and pore volume of nanocatalysts were given in Figure 2 and Table 3. In this study, all of the used nanocatalysts were exhibited the V-type adsorption-desorption isotherm with H1 type hysteresis loop [51]. This indicates that the catalysts are mesoporous in according to International Union of Pure and Applied Chemistry (IUPAC) categorization. BET surface areas of Au/MWCNT, Bi/MWCNT, and Au$_{80}$Bi$_{20}$/MWCNT were found as 159.0, 225.1, and 221.6 m^2/g, respectively. As can be clearly seen from Table 3, the use of Bi and Au together increased the BET surface area. Likewise, the increase in pore volume and pore size of the nanocatalyst were observed (Table 3). According to the pore size and pore volume, the nanocatalysts are sorted Au$_{80}$Bi$_{20}$/MWCNT > Bi/MWCNT > Au/MWCNT.

The morphological and particle size of the Au/MWCNT, Bi/MWCNT, and Au$_{80}$Bi$_{20}$/MWCNT nanocatalysts was determined with TEM and were depicted in Figure 3. It is explicit that Au and Bi nanoparticles were agglomerated for Au/MWCNT and Bi/MWCNT nano-catalysts. However, it can be clearly seen that such a situation is not observed for Au$_{80}$Bi$_{20}$/MWCNT nanocatalyst and that there is a homogeneous distribution. This can be explained by the fact that Bi nanoparticles on the MWCNT surface have a positive effect by entering between the Au nanoparticles. The increase in BET surface area of Au$_{80}$Bi$_{20}$/MWCNT compared to Au/CNT could support this positive effect. The average particle size for Au/MWCNT, Bi/MWCNT, and Au$_{80}$Bi$_{20}$/MWCNT nanocatalysts was found as 26.8, 23.2, and 19.38 nm, respectively. The particle size for Au$_{80}$Bi$_{20}$/MWCNT was found to be consistent with crystal sizes obtained from the XRD result.
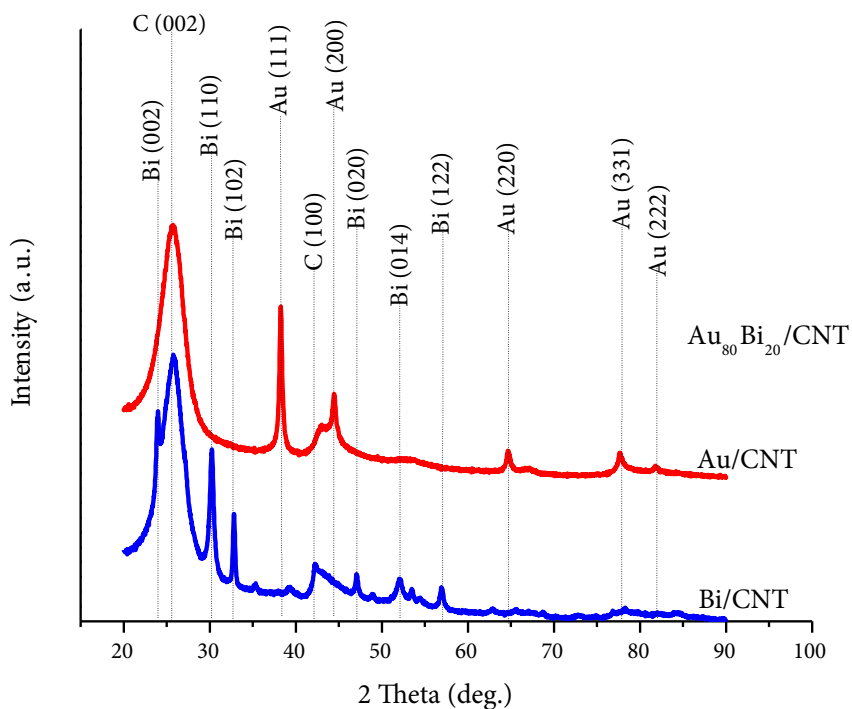
Figure 1. The XRD patterns of the monometallic Bi/MWCNT, Au/MWCNT, and bimetallic $Au_{80}Bi_{20}$/MWCNT nanocatalysts.
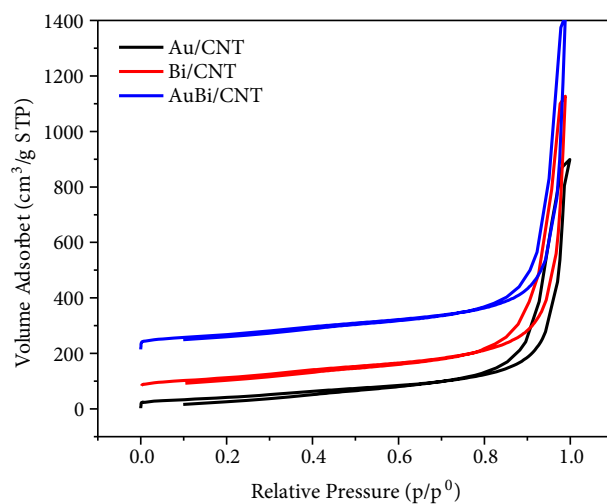
Figure 2. N_2 adsorption-desorption isotherms of Au/MWCNT, Bi/MWCNT, and $Au_{80}Bi_{20}$/MWCNT nanocatalysts.

Table 3. Summary of the BET of result of Au/MWCNT, Bi/MWCNT, and $Au_{80}Bi_{20}$/MWCNT.

Nanocatalyst	BET surface area (m²/g)	Pore volume (cm³/g)	Pore size (nm)
Au/MWCNT	159.0	1.23	24.5
Bi/MWCNT	225.1	1.65	25.6
$Au_{80}Bi_{20}$/MWCNT	221.6	1.86	28.7
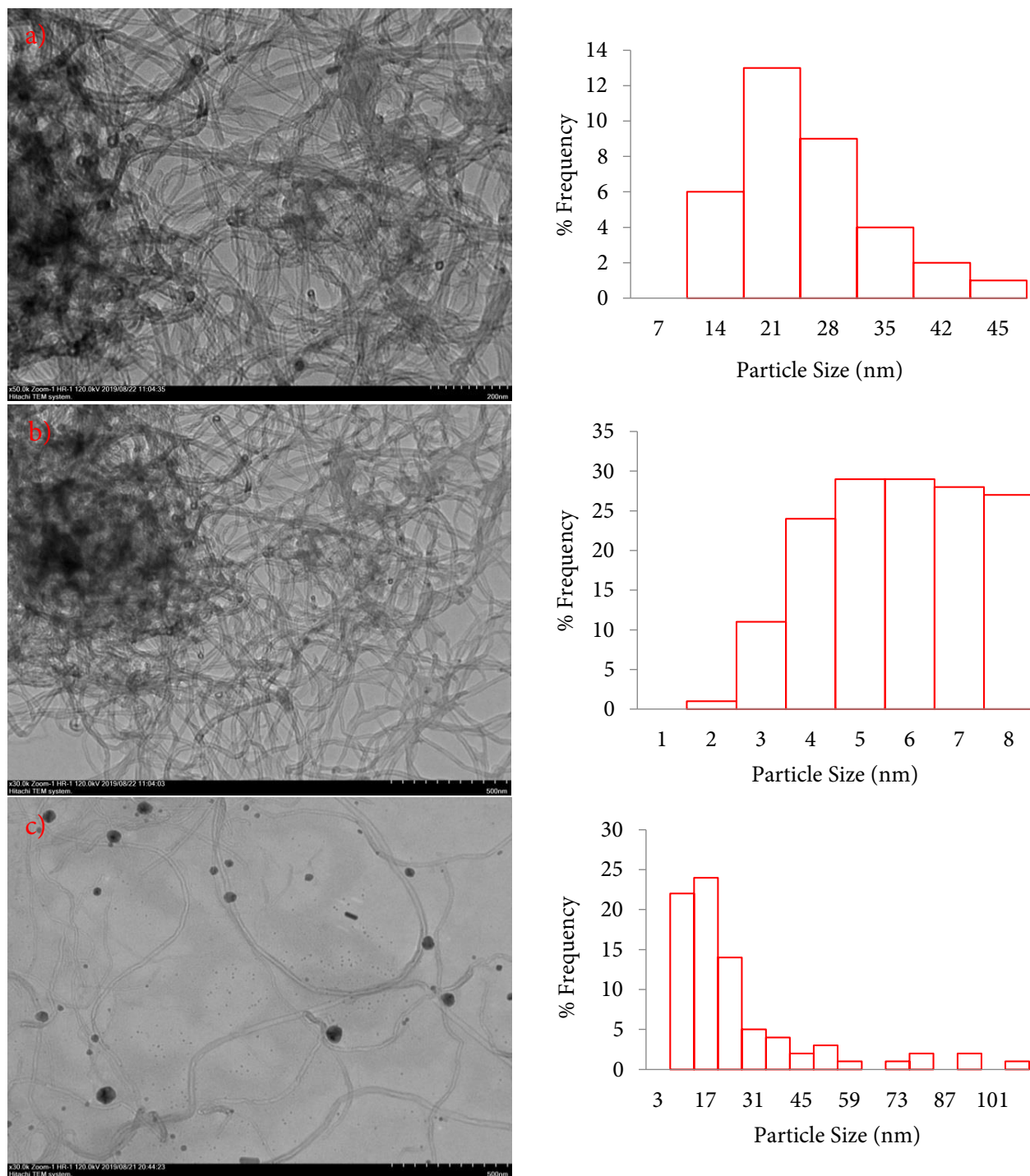
Figure 3. TEM images of (a and b) $Au_{80}Bi_{20}$/MWCNT, (c and d) Au/MWCNT, and (e and f) Bi/MWCNT nano-catalysts (corresponding histogram of particle size distribution).

3.2. Electrochemical assessment

Au/MWCNT, Bi/MWCNT, and Au-Bi/MWCNT nanocatalysts were prepared via the $NaBH_4$ reduction method to investigate their GAEO activity. Figure 4 depicts electrooxidation measurement of Au/MWCNT, Bi/MWCNT, and Au-Bi/MWCNT in 0.5 GA solution. Synthesized nanocatalysts were tested in 1 M KOH and 0.5 M GA, respectively. In this way, the best atomic molar ratios were determined and the second stage was passed.
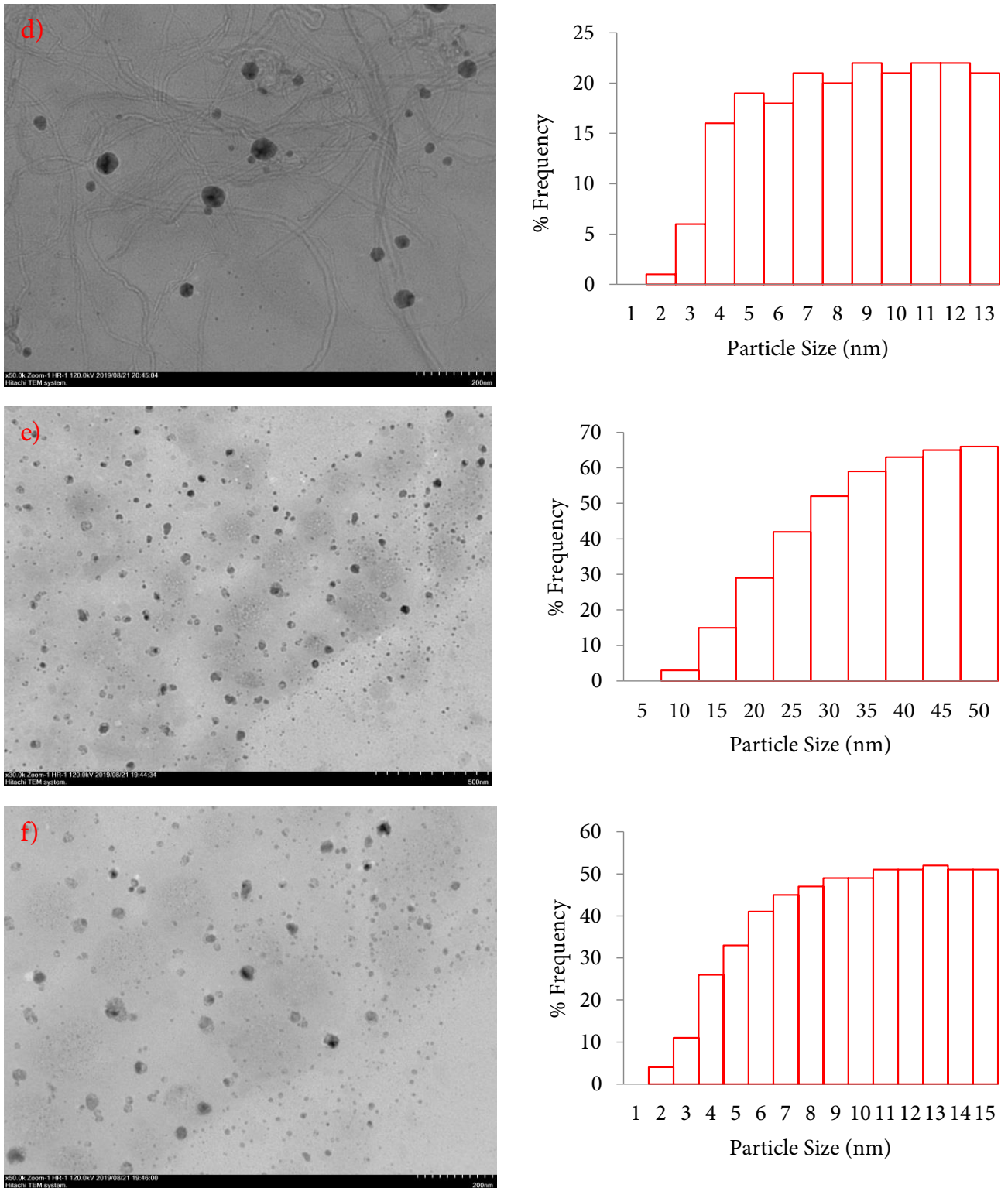
Figure 3. (Continued).

The hydroxide (OH⁻) adsorption-desorption peak was observed for Au and Bi between 0.4 V and 0.6 V, while these peaks were not visible for $Au_{80}Bi_{20}$ (Figure 4a). As described in the literature, the Au desorption peak is obtained due to the reduction of the oxidative gold layer [52]. Due to the dispersion of Bi nanoparticles in the Au layer formed on the
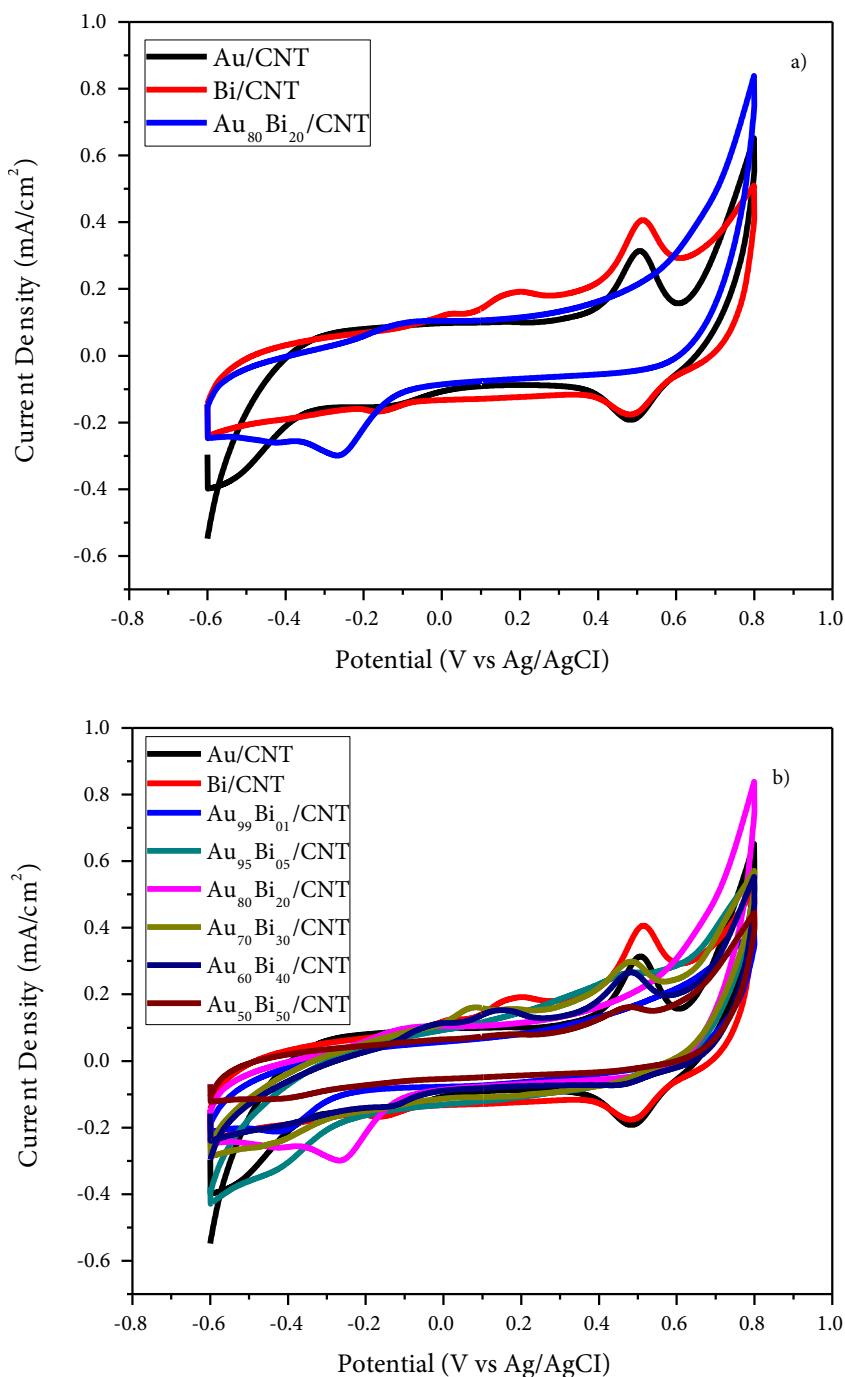
Figure 4. Cyclic voltammograms in 1 M KOH for electrodes modified with a) 3% Au/MWCNT, 3% Bi/MWCNT, and 3% $Au_{80}Bi_{20}$/MWCNT nanocatalysts; b) 3% Au/MWCNT, 3% Bi/MWCNT, and 3% AuBi/MWCNT nano-catalysts (scan rate: 50 mV s^{-1}).

surface of the AuBi/MWCNT nanocatalyst, it could prevent oxidation at the positive forward direction peak of the Au layer. As seen, electrooxidation peaks were obtained for all nanocatalysts prepared. When using Bi together with Au, it is observed that the current density is clearly increased. $Au_{80}Bi_{20}$/MWCNT nanocatalyst exhibited the highest performance among prepared nanocatalysts with 1.133 mA/cm² (320.1 mA/mg Au) for GAEO (Figure 5 and Table 4). These results are consistent with CA and EIS measurements.
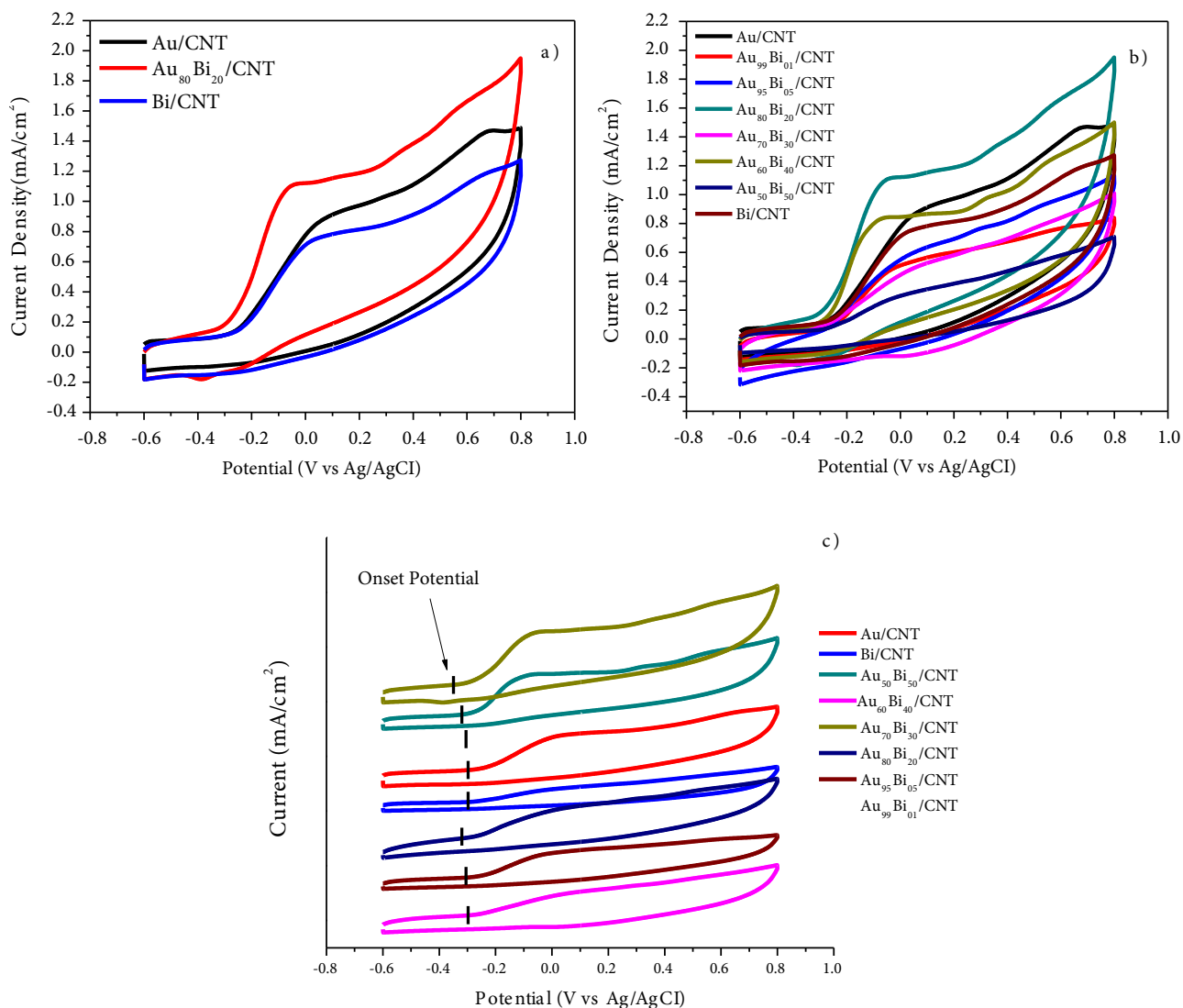
Figure 5. Cyclic voltammograms in 1 M KOH + 0.5 M GA for electrodes modified with a) 3% Au/MWCNT, 3% Bi/MWCNT, and 3% Au$_{80}$Bi$_{20}$/MWCNT nanocatalysts; b) 3% Au/MWCNT, 3% Bi/MWCNT, and 3% AuBi/MWCNT nanocatalysts; c) onset potentials of all nanocatalysts (scan rate: 50 mV s^{-1}).

Table 4. Electrochemical properties of synthesized nanocatalysts for GAEO.

Nanocatalyst	Peak potential of forward peak, V	Specific activity, mA/cm^2	Mass activity, mA/mg Pd	Onset potential, V
Au/MWCNT	0.103	0.936	256.5	−0.291
Bi/MWCNT	0.036	0.764	202.3	−0.307
AuBi(99:01)/MWCNT	0.016	0.519	142.3	−−0.264
AuBi(95:05)/MWCNT	0.026	0.595	159.4	−0.269
AuBi(80:20)/MWCNT	−0.039	1.133	320.1	−0.345
AuBi(70:30)/MWCNT	0.057	0.510	134.7	−0.307
AuBi(60:40)/MWCNT	−0.060	0.840	232.6	−0.309
AuBi(50:50)/MWCNT	−0.014	0.302	84.5	−0.258

The mass activities of Au/MWCNT, Bi/MWCNT, and $Au_{80}Bi_{20}$/MWCNT catalysts were examined via LSV technique at a scan rate of 50 mV s^{-1}. LSV profile of these nanocatalysts in 1 M KOH + 0.5 M GA solution were given in Figure 6. As could be seen in Figure 6, $Au_{80}Bi_{20}$/MWCNT nanocatalyst exhibited a higher mass activity compared to these of Au/MWCNT and Bi/MWCNT nanocatalysts toward GA electrooxidation. Mass activities over the total potential for Au/MWCNT, Bi/MWCNT, and $Au_{80}Bi_{20}$/MWCNT were determined as 1024.60, 200.82, and 1601.64 mA/mg Au, respectively. These results were consistent with the results from CV, CA, and EIS.

Electrode preparation parameters for maximum glucose electrooxidation, namely V_c, t_u, and t_d were optimized by using RSM. In optimization studies, the working electrode was modified with the AuBi nanocatalyst. Table 2 exhibits the experimental design from CCD and corresponding response values. The obtained data depict that the GAEO on AuBi can be modeled well with the quadratic regression model at determined conditions. Accordingly, Eqn. 4 and Eqn. 5 depict model equations for GAEO consisting of real and coded factors, respectively.

Specific Activity = 1.01−0.12 A+0.14B−0.024 C−0.097AB+0.045AC+0.005BC+0.22A^2−0.24B^2−0.13AC^2 (4)

Specific Activity = 0.79335−0.073089 V_c + 0.025536 t_u + 0.014417 t_d -0.000455874 $V_c t_u$ +0.000428062 $V_c t_d$ − 0.0000116891 $t_u t_d$ + 0.00410766 V_c^2 − 0.000280484 t_u^2−0.000613988 t_d^2 (5)

The adequacy and significance of the model were validated with analysis of variance (ANOVA). The ANOVA results depict that the P-value of the model is less than 0.05, and this indicates that the model is statistically significant (Table 5). Besides, the determination of coefficient and adequate precision values of the model were found to be 0.89 and 10.7, respectively. The fact that the lack of fit value was statistically insignificant indicates that the model depicts a good agreement with the experimental data. Accordingly, the proposed model can be utilized to navigate the design space [53].

Figure 8 depicts the response surface plots for t_u, V_c and t_d parameters. The interaction between t_u and V_c for specific activity toward GAEO was presented in Figure 8a. Specific activity for GAEO decreases when the V_c value is increased from 0.5 to 7.75 μL. An increase in specific activity was observed for nanocatalyst loads higher than 7.75 μL. Figure 8b depicts that the specific activity increases up to about 15 min of t_d and begins to decrease after this maximum point. It was observed that the AuBi nanocatalyst could not attach enough to the electrode surface at very low t_d values, and some of the nanocatalysts were removed from the electrode surface. At higher t_d values, lower specific activities were observed as a result of oxidation of metals and vaporizing of Nafion in the nanocatalyst slurry. It was determined from Figure 8c that the relation of the specific activity with t_u depicts a volcano shape. The specific activity of AuBi for GAEO increased up to about 45 min of t_u, and a decrease was observed after this value. This may be due to the sonification time affecting the
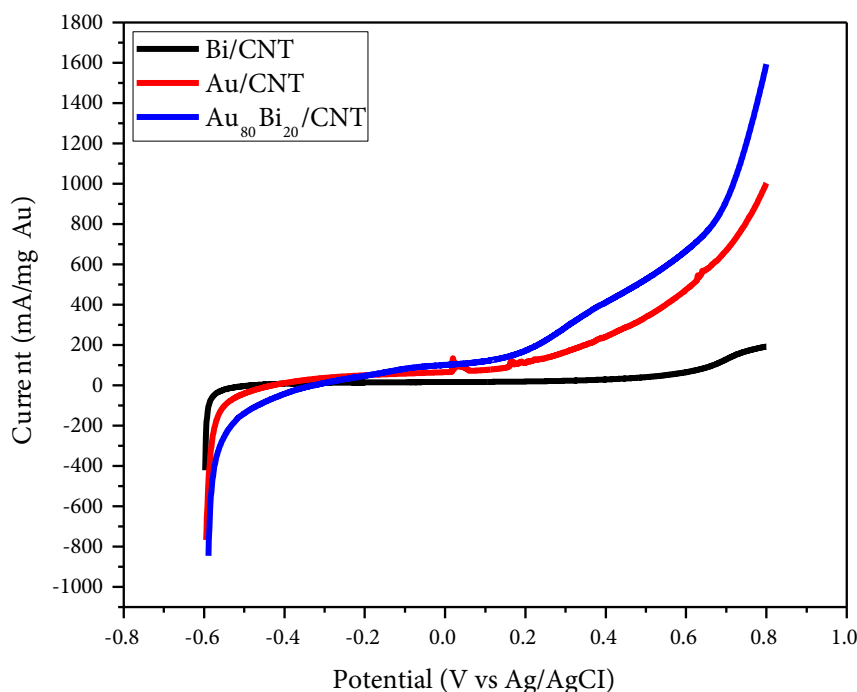
Figure 6. LSV profiles of 3% Au/MWCNT, 3% Bi/MWCNT, and 3% $Au_{80}Bi_{20}$/MWCNT nanocatalysts in 1 M KOH + 0.5 M GA for modified electrode.

Table 5. ANOVA regression model for GAEO.

Source	Sum of Squares	df	Mean Square	F-value	p-value	
Model	0.76	9	0.084	9.27	0.0009	significant
A-Volume of nanocatalyst mixture	0.15	1	0.15	16.11	0.0025	
B-Ultrasonification of nanocatalyst mixture	0.19	1	0.19	21.26	0.0010	
C-Duration of drying	0.00576	1	0.00576	0.63	0.4444	
AB	0.076	1	0.076	8.37	0.0160	
AC	0.016	1	0.016	1.78	0.2114	
BC	0.0002	1	0.0002	0.022	0.8850	
A^2	0.13	1	0.13	14.11	0.0037	
B^2	0.16	1	0.16	18.03	0.0017	
C^2	0.046	1	0.046	5.04	0.0485	
Residual	0.091	10	0.009086			
Lack of Fit	0.057	5	0.011	1.71	0.2852	not significant
Pure error	0.034	5	0.006707			
Cor total	0.85	19				
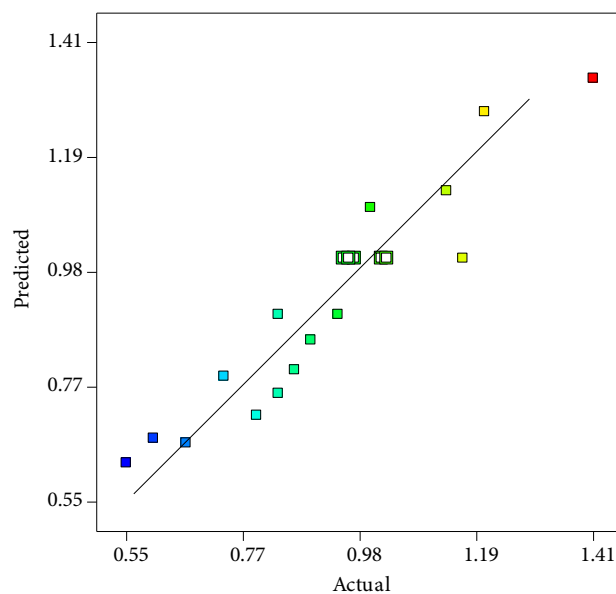
Figure 7. Comparison of experimental and predicted values for GAEO.

crystal structures of the nanoparticles. Pollet et al. emphasized that during high sonification periods, the crystallinity of nanoparticles can be disrupted, and the formation of amorphous structures could be observed [54].

Design-Expert software was used to determine optimum conditions for GAEO, and related results were summarized in Table 6. The V_c of 0.5 µL, t_u of 44.87 min, and t_d of 11.49 min were obtained as an optimum condition for electrode preparation toward GAEO on AuBi/MWCNT. It could be seen in Table 6 that specific activity under optimum conditions was predicted by the obtained model as 1.40971 mA/cm². The experiment was conducted under optimum conditions to verify the specific activity value derived from the model, and the specific activity was found to be 1.62 mA/cm². It was determined that the obtained model was close to the experimental value with an error of 13%, indicating that the predicted value was in harmony with the observed value.
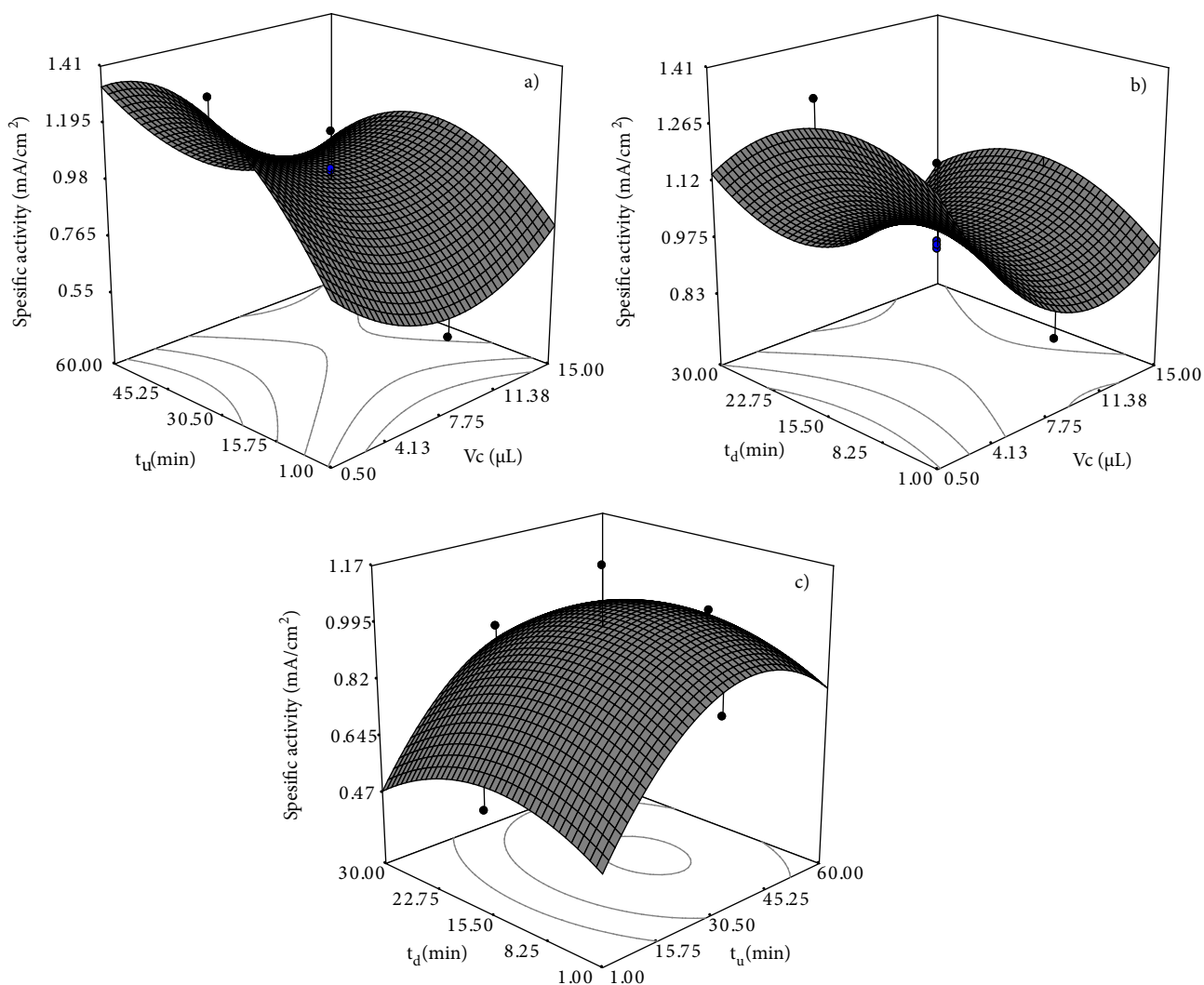
Figure 8. Response surface plots of a) t_u and V_c, b) t_d and V_c, and c) t_d and t_u for GAEO.

Table 6. Optimum conditions by the CCD.

Number	V_c (µL)	t_u (min)	t_d (min)	Spesific activity (mA/cm²)	Desirability
1	0.50	44.87	11.49	1.40971	1.000
2	0.50	42.63	12.83	1.40723	0.997
3	0.50	49.08	13.28	1.4027	0.992
4	0.50	46.53	14.81	1.40211	0.991
5	0.50	42.17	17.43	1.38618	0.972
6	15.00	32.98	16.67	1.10313	0.643
7	15.00	32.85	16.79	1.10311	0.643
8	15.00	33.83	17.28	1.10268	0.643

The stability and GAEO activity of synthesized nanocatalysts were determined via CA. Figure 9a depicts CA results of Au/MWCNT, Bi/MWCNT, and $Au_{80}Bi_{20}$/MWCNT in 0.5 M GA at −0.4 V potential. Figure 9b depicts the currents at the end of 1000 s. At the end of 1000 s, $Au_{80}Bi_{20}$/MWCNT current value is approximately 1.4 and 1.8 times greater than Au/
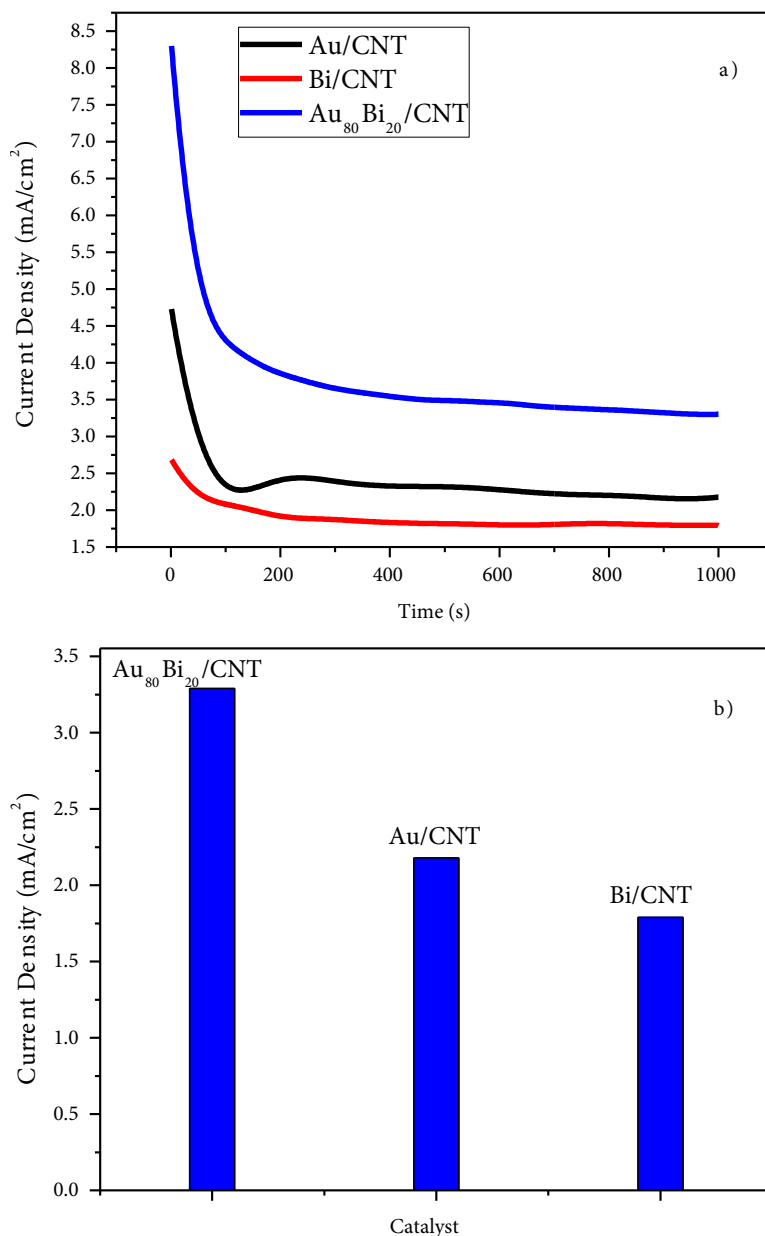
Figure 9. Chronoamperomograms of Au/MWCNT, Bi/MWCNT, and $Au_{80}Bi_{20}$/MWCNT in 0.5 M GA at -0.4 V.

MWCNT and Bi/MWCNT, respectively. Moreover, $Au_{80}Bi_{20}$/MWCNT has the best stability and highest GAEO activity in the long term.

Figure 10 depicts the Nyguist plot for Au/MWCNT, Bi/MWCNT, and AuBi/MWCNT in 0.5 M GA. The shape of the Nyguist plots is generally semicircle, and the diameter of these semicircles has a significant effect on the charge transfer resistance of catalyst. Accordingly, when the diameter of the semicircles decreases, the charge transfer resistance decreases and the GAEO activity of the nanocatalyst increases. According to Figure 10, the charge transfer resistance can be listed as $Au_{80}Bi_{20}$/MWCNT <Au/MWCNT <Bi/MWCNT. The fitted EIS profile of Au/MWCNT, Bi/MWCNT, and AuBi/MWCNT were given in Figure S1, Figure S2, and Figure S3, respectively. The charge transfer resistance of Au/MWCNT, Bi/MWCNT, and AuBi/MWCNT were determined as 2.502, 3.733, and 2.279 Ω, respectively. As a result, it was found that $Au_{80}Bi_{20}$/MWCNT nanocatalyst has the highest GAEO activity, and these results are in agreement with CV and CA results.
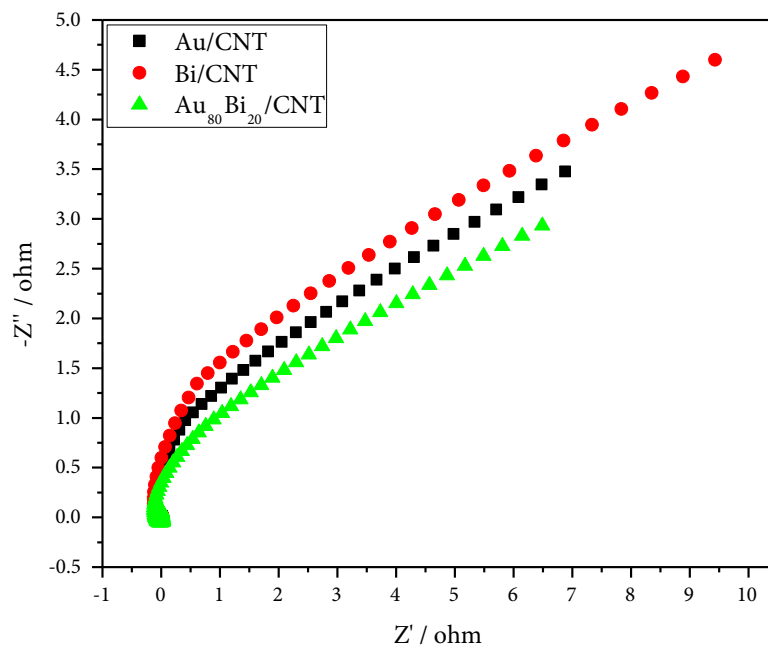
Figure 10. Nyquist plots obtained in 0.5 M GA for electrodes modified with Au/MWCNT, Bi/MWCNT, and $Au_{80}Bi_{20}$/MWCNT at –0.1 V.

4. Conclusion

Au/MWCNT, Bi/MWCNT, and bimetallic Au-Bi/MWCNT were synthesized via $NaBH_4$ reduction method, characterized by advanced surface analytical methods. The electrocatalytic performance of prepared catalyst was investigated with EIS, CV, CA, and LSV toward GAEO. Following results and insights were obtained:

Ø   Au/MWCNT, Bi/MWCNT, and Au-Bi/MWCNT at varying Au:Bi ratios could be easily prepared from corresponding Au and Bi precursors via $NaBH_4$ reduction method.

Ø   According to XRD and TEM results, particle sizes of $Au_{80}Bi_{20}$/MWCNT were compatible with each other. It was observed that the BET surface area of Au/MWCNT increased with the addition of Bi.

Ø   Electrochemical measurement was revealed that Bi addition improves the electrochemical activity of Au/MWCNT. This situation can be explained by electronic effect.

Ø   According to CV results, $Au_{80}Bi_{20}$/MWCNT showed the highest GAEO performance. The optimum metal molar ratio is the basis for this performance.

Ø   CCD was utilized for optimum conditions of the electrode preparation. The volume of nanocatalyst slurry (V_c, A), ultrasonication time of the nanocatalyst slurry (t_u, B), and the drying time of the electrode (t_d, C) are determined as independent variables. The maximum current density values obtained for GAEO were identified as the response. The V_c of 0.5 µL, t_u of 44.87 min, and t_d of 11.49 min were obtained as an optimum condition for electrode preparation toward GAEO on AuBi/MWCNT.

Ø   CA and EIS results revealed that AuBi nanocatalyst has a high stability and fast oxidation kinetics.

Ø   The data obtained from this study depicts that $Au_{80}Bi_{20}$/MWCNT nanocatalyst is a good candidate as anode nanocatalyst for DGFC.

References

1.   Ulas B, Caglar A, Sahin O, Kivrak H. Composition dependent activity of PdAgNi alloy catalysts for formic acid electrooxidation. Journal of Colloid and Interface Science 2018; 532: 47-57. doi: 10.1016/j.jcis.2018.07.120

2. Kucukvar M, Onat NC, Haider MA. Material dependence of national energy development plans: The case for Turkey and United Kingdom. Journal of Cleaner Production 2018; 200: 490-500. doi: 10.1016/j.jclepro.2018.07.245

3. Ozgür T, Yakaryılmaz AC. A review: exergy analysis of PEM and PEM fuel cell based CHP systems. International Journal of Hydrogen Energy 2018; 43 (38): 17993-8000. doi: 10.1016/j.ijhydene.2018.01.106

4. Kakaei K, Khodadoost S, Gholipour M, Shouraei N. Core-shell polyaniline functionalized carbon quantum dots for supercapacitor. Journal of Physics and Chemistry of Solids 2021; 148: 109753. doi: 10.1016/j.jpcs.2020.109753

5. Kakaei K, Ghadimi G. A green method for Nitrogen-doped graphene and its application for oxygen reduction reaction in alkaline media. Materials Technology 2021; 36 (1): 46-53. doi: 10.1080/10667857.2020.1724692

6. Kakaei K, Ostadi Z. Nickel nanoparticles coated on the exfoliated graphene layer as an efficient and stable catalyst for oxygen reduction and hydrogen evolution in alkaline media. Materials Research Express 2020; 7 (5): 055504. doi: 10.1088/2053-1591/ab8c70

7. Yayla S, Ayça S, Oruç M. A case study on piezoelectric energy harvesting with using vortex generator plate modeling for fluids. Renewable Energy 2020; 157: 1243-1253. doi: 10.1016/j.renene.2020.05.027

8. Kivrak H, Atbas D, Alal O, Çögenli MS, Bayrakceken A et al. A complementary study on novel PdAuCo catalysts: Synthesis, characterization, direct formic acid fuel cell application, and exergy analysis. International Journal of Hydrogen Energy 2018; 43 (48): 21886-21898. doi: 10.1016/j.ijhydene.2018.09.135

9. Caglar A, Sahan T, Cogenli MS, Yurtcan AB, Aktas N et al. A novel central composite design based response surface methodology optimization study for the synthesis of Pd/CNT direct formic acid fuel cell anode catalyst. International Journal of Hydrogen Energy 2018; 43 (24): 11002-11011. doi: 10.1016/j.ijhydene.2018.04.208

10. Er OM, Caglar A, Ulas B, Kivrak H, Kivrak A. Novel carbon nanotube supported Co@Ag@Pd formic acid electrooxidation catalysts prepared via sodium borohydride sequential reduction method. Materials Chemistry and Physics 2019; 241: 122422. doi: 10.1016/j.matchemphys.2019.122422

11. Tao B, Miao F, Chu PK. Preparation and characterization of a novel nickel–palladium electrode supported by silicon nanowires for direct glucose fuel cell. Electrochimica Acta 2012; 65: 149-152. doi: 10.1016/j.electacta.2012.01.017

12. Silva LS, Almeida CV, Meneses CT, Batista EA, Santos SF et al. AuPd/C core–shell and alloy nanoparticles with enhanced catalytic activity toward the electro-oxidation of ethanol in alkaline media. Applied Catalysis B: Environmental 2019; 251: 313-325. doi: 10.1016/j.apcatb.2019.03.067

13. Kakaei K, Rahnavardi M. Synthesis of nitrogen-doped reduced graphene oxide and its decoration with high efficiency palladium nanoparticles for direct ethanol fuel cell. Renewable Energy 2021; 163: 1277-1286. doi: 10.1016/j.renene.2020.09.043

14. Zhang Y, Gao F, Song P, Wang J, Song T et al. The chain-typed nanoflowers structure endows PtBi with highly electrocatalytic activity of ethylene glycol oxidation. Journal of Alloys and Compounds 2019; 789: 834-840. doi: 10.1016/j.jallcom.2019.03.067

15. Zabielaitė A, Balčiūnaitė A, Šimkūnaitė D, Lichušina S, Stalnionienė I et al. High performance direct N_2H_4-H_2O_2 fuel cell using fiber-shaped co decorated with Pt crystallites as anode electrocatalysts. Journal of the Electrochemical Society 2020; 167 (5): 054502. doi: 10.1149/2.0052005jes

16. Chuesutham T, Sirivat A, Paradee N, Changkhamchom S, Wattanakul K et al. Improvement of sulfonated poly (ether ether ketone)/Y zeolite-SO_3H via organo-functionalization method for direct methanol fuel cell. Renewable Energy 2019; 138: 243-249. doi: 10.1016/j.renene.2019.01.107

17. Kakaei K, Javan H, Mohammadi HB. Synthesis of carbon quantum dots nanoparticles by cyclic voltammetry and its application as methanol tolerant oxygen reduction reaction electrocatalyst. Journal of the Chinese Chemical Society 2016; 63 (5): 432-437. doi: 10.1002/jccs.201500534

18. Chen J, Zhao CX, Zhi MM, Wang K, Deng L et al. Alkaline direct oxidation glucose fuel cell system using silver/nickel foams as electrodes. Electrochimica Acta 2012; 66: 133-138. doi: 10.1016/j.electacta.2012.01.071

19. Caglar A, Ulas B, Sahin O, Kivrak H. Synthesis of in situ N-, S-, and B-doped few-layer graphene by chemical vapor deposition technique and their superior glucose electrooxidation activity. International Journal of Energy Research 2019; 43 (14): 8204-8216. doi: 10.1002/er.4817

20. El-Nagar GA, Derr I, Fetyan A, Roth C. One-pot synthesis of a high performance chitosan-nickel oxyhydroxide nanocomposite for glucose fuel cell and electro-sensing applications. Applied Catalysis B: Environmental 2017; 204: 185-199. doi: 10.1016/j.apcatb.2016.11.031

21. Song BY, Li YS, He YL, Cheng ZD. Anode structure design for the high-performance anion-exchange membrane direct glucose fuel cell. Energy Procedia 2014; 61: 2118-2122. doi: 10.1016/j.egypro.2014.12.089

22. Basu D, Basu S. Performance studies of Pd–Pt and Pt–Pd–Au catalyst for electro-oxidation of glucose in direct glucose fuel cell. International Journal of Hydrogen Energy 2012; 37 (5): 4678-4684. doi: 10.1016/j.ijhydene.2011.04.158

23. Kerzenmacher S, Ducrée J, Zengerle R, Von Stetten F. Energy harvesting by implantable abiotically catalyzed glucose fuel cells. Journal of Power Sources 2008; 182 (1): 1-17. doi: 10.1016/j.jpowsour.2008.03.031

24. Yang YL, Liu XH, Hao MQ, Zhang PP. Performance of a low-cost direct glucose fuel cell with an anion-exchange membrane. International Journal of Hydrogen Energy 2015; 40 (34): 10979-10984. doi: 10.1016/j.ijhydene.2015.05.192

25. Navaee A, Narimani M, Korani A, Ahmadi R, Salimi A, et al. Bimetallic $Fe_{15}Pt_{85}$ nanoparticles as an effective anodic electrocatalyst for non-enzymatic glucose/oxygen biofuel cell. Electrochimica Acta 2016; 208: 325-333. doi: 10.1016/j.electacta.2016.05.033

26. Eshghi A. Graphene/Ni–Fe layered double hydroxide nano composites as advanced electrode materials for glucose electro oxidation. International Journal of Hydrogen Energy 2017; 42 (22): 15064-15072. doi: 10.1016/j.ijhydene.2017.04.288

27. Gao M, Liu X, Irfan M, Shi J, Wang X et al. Nickle-cobalt composite catalyst-modified activated carbon anode for direct glucose alkaline fuel cell. International Journal of Hydrogen Energy 2018; 43 (3): 1805-1815. doi: 10.1016/j.ijhydene.2017.11.114

28. Li L, Scott K, Yu EH. A direct glucose alkaline fuel cell using MnO_2–carbon nanocomposite supported gold catalyst for anode glucose oxidation. Journal of Power Sources 2013; 221: 1-5. doi: 10.1016/j.jpowsour.2012.08.021

29. Lemoine C, Dubois L, Napporn TW, Servat K, Kokoh KB. Electrochemical energy conversion from direct oxidation of glucose on active electrode materials. Electrocatalysis 2019; 11: 170–179. doi: 10.1007/s12678-019-00570-1

30. Caglar A, Ulas B, Sahin O, Kivrak H. Few-layer graphene coated on indium tin oxide electrodes prepared by chemical vapor deposition and their enhanced glucose electrooxidation activity. Energy Storage 2019; 1 (4): e73. doi: 10.1002/est2.73

31. Huynh TTK, Tran TQN, Yoon HH, Kim W-J, Kim IT. AgNi@ ZnO nanorods grown on graphene as an anodic catalyst for direct glucose fuel cells. Korean Journal of Chemical Engineering 2019; 36 (7): 1193-1200. doi: 10.1007/s11814-019-0293-z

32. Song S, Wang K, Yan L, Brouzgou A, Zhang Y et al. Ceria promoted Pd/C catalysts for glucose electrooxidation in alkaline media. Applied Catalysis B: Environmental 2015; 176: 233-239. doi: 10.1016/j.apcatb.2015.03.059

33. Dong F, Liu X, Irfan M, Yang L, Li S et al. Macaroon-like $FeCo_2O_4$ modified activated carbon anode for enhancing power generation in direct glucose fuel cell. International Journal of Hydrogen Energy 2019; 44 (16): 8178-8187. doi: 10.1016/j.ijhydene.2019.02.031

34. Rafaïdeen T, Baranton S, Coutanceau C. Highly efficient and selective electrooxidation of glucose and xylose in alkaline medium at carbon supported alloyed PdAu nanocatalysts. Applied Catalysis B: Environmental 2019; 243: 641-656. doi: 10.1016/j.apcatb.2018.11.006

35. Chai D, Zhang X, Chan SH, Li G. Facile aqueous phase synthesis of Pd_3Cu–B/C catalyst for enhanced glucose electrooxidation. Journal of the Taiwan Institute of Chemical Engineers 2019; 95: 139-146. doi: 10.1016/j.jtice.2018.10.009

36. Yan L, Brouzgou A, Meng Y, Xiao M, Tsiakaras P et al. Efficient and poison-tolerant Pd_xAu_y/C binary electrocatalysts for glucose electrooxidation in alkaline medium. Applied Catalysis B: Environmental 2014; 150: 268-274. doi: 10.1016/j.apcatb.2013.12.026

37. Chai D, Wang W, Wang F, Kang Y, Yang Y et al. A facile precipitation procedure for synthesis of binary Sn-Co oxide promoting Pd catalyst towards glucose electrooxidation. Electrochima Acta 2016; 189: 295-302. doi: 10.1016/j.electacta.2015.12.071

38. Brouzgou A, Yan L, Song S, Tsiakaras P. Glucose electrooxidation over Pd_xRh/C electrocatalysts in alkaline medium. Applied Catalysis B: Environmental 2014; 147: 481-489. doi: 10.1016/j.apcatb.2013.09.024

39. Cuevas-Muñiz F, Guerra-Balcázar M, Castaneda F, Ledesma-García J, Arriaga L. Performance of Au and AuAg nanoparticles supported on Vulcan in a glucose laminar membraneless microfuel cell. Journal of Power Sources 2011; 196 (14): 5853-5857. doi: 10.1016/j.jpowsour.2011.02.081

40. Brouzgou A, Song S, Tsiakaras P. Carbon-supported PdSn and Pd_3Sn_2 anodes for glucose electrooxidation in alkaline media. Applied Catalysis B: Environmental. 2014; 158: 209-216. doi: 10.1016/j.apcatb.2014.03.051

41. Basu D, Basu S. A study on direct glucose and fructose alkaline fuel cell. Electrochima Acta 2010; 55 (20): 5775-5779. doi: 10.1016/j.electacta.2010.05.016

42. Basu D, Basu S. Synthesis, characterization and application of platinum based bimetallic catalysts for direct glucose alkaline fuel cell. Electrochimica Acta 2011; 56 (17): 6106-6113. doi: 10.1016/j.electacta.2011.04.072

43. Ji Y, Liu J, Liu X, Yuen MM, Fu X-Z et al. 3D porous Cu@ Cu_2O films supported Pd nanoparticles for glucose electrocatalytic oxidation. Electrochima Acta 2017; 248: 299-306. doi: 10.1016/j.electacta.2017.07.100

44. Kivrak H, Alal O, Atbas D. Efficient and rapid microwave-assisted route to synthesize $Pt–MnO_x$ hydrogen peroxide sensor. Electrochima Acta 2015; 176: 497-503. doi: 10.1016/j.electacta.2015.06.151

45. Geng G, Chen P, Guan B, Liu Y, Yang C et al. Sheetlike gold nanostructures/graphene oxide composites via a one-pot green fabrication protocol and their interesting two-stage catalytic behaviors. The Royal Society of Chemistry Advance 2017; 7 (82): 51838-51846. doi: 10.1039/C7RA11188F

46. Ballarin B, Cassani M, Tonelli D, Boanini E, Albonetti S et al. Gold nanoparticle-containing membranes from in situ reduction of a gold (III)– aminoethylimidazolium aurate salt. The Journal of Physical Chemistry C 2010; 114 (21): 9693-9701. doi: 10.1021/jp1024262

47. Lin YC, Lee MW. Bi_2S_3 liquid-junction semiconductor-sensitized SnO_2 solar cells. Journal of the Electrochemical Society 2014; 161 (1): H1-H5. doi: 10.1149/2.002401jes

48. Akbari A, Khammar M, Taherzadeh D, Rajabian A, Zak AK et al. Zinc-doped cerium oxide nanoparticles: sol-gel synthesis, characterization, and investigation of their in vitro cytotoxicity effects. Journal of Molecular Structure 2017; 1149: 771-776. doi: 10.1016/j.molstruc.2017.08.069

49. Arbag H, Tasdemir HM, Yagizatli Y, Kucuker M, Yasyerli S. Effect of preparation technique on the performance of Ni and Ce incorporated modified alumina catalysts in CO_2 reforming of methane. Catalysis Letters 2020; 150 (11): 3256-3268. doi: 10.1007/s10562-020-03228-6

50. Kakaei K, Hamidi M, Kakaei N. Simultaneous electro-synthesis of polyaniline graphene nanocomposite in dilute graphene oxide as dopant and aniline by electrochemical method and its high specific capacitance. Materials Research Express 2019; 6 (8): 085623. doi: 10.1088/2053-1591/ab2312

51. Sing KS, Williams RT. Physisorption hysteresis loops and the characterization of nanoporous materials. Adsorption Science & Technology 2004; 22 (10): 773-782. doi: 10.1260/0263617053499032

52. Basu D, Basu S. Synthesis and characterization of Pt–Au/C catalyst for glucose electro-oxidation for the application in direct glucose fuel cell. International Journal of Hydrogen Energy 2011; 36 (22): 14923-14929. doi: 10.1016/j.ijhydene.2011.03.042

53. Bagheri R, Ghaedi M, Asfaram A, Alipanahpour Dil E, Javadian H. RSM-CCD design of malachite green adsorption onto activated carbon with multimodal pore size distribution prepared from Amygdalus scoparia: kinetic and isotherm studies. Polyhedron 2019; 171: 464-472. doi: 10.1016/j.poly.2019.07.037

54. Pollet BG. The use of ultrasound for the fabrication of fuel cell materials. International Journal of Hydrogen Energy 2010; 35 (21): 11986-12004. doi: 10.1016/j.ijhydene.2010.08.021
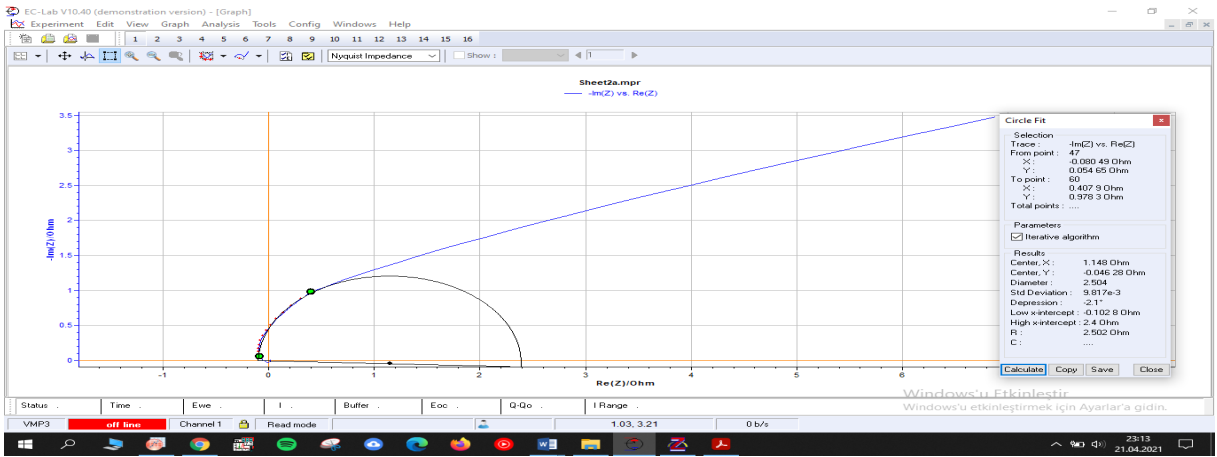
Figure S1. Fitted EIS profile of Au/CNT.
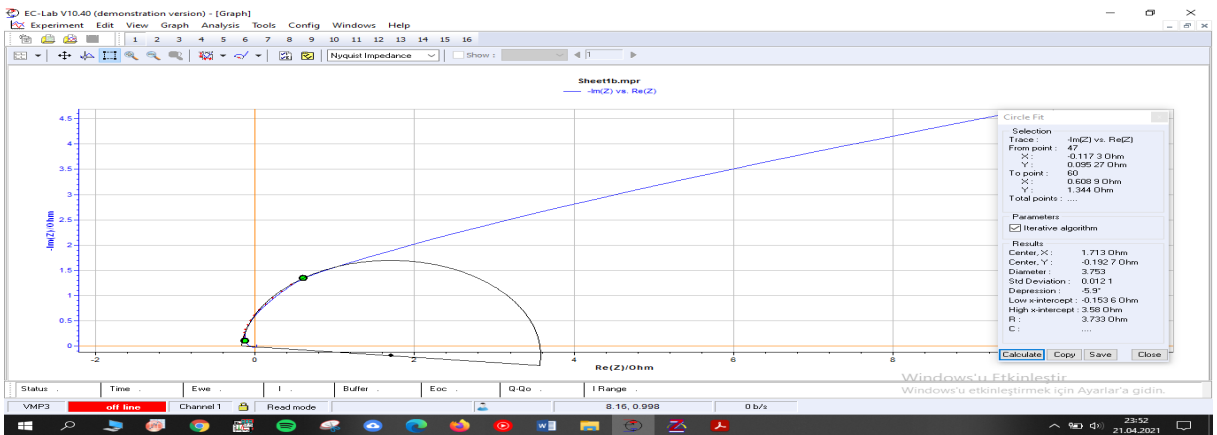
Figure S2. Fitted EIS profile of Bi/CNT.

Figure S3. Fitted EIS profile of AuBi/CNT.